nature ecology & evolution

Article

https://doi.org/10.1038/s41559-024-02372-1

Climate-induced tree-mortality pulses are obscured by broad-scale and long-term greening

Received: 26 November 2022

Accepted: 16 February 2024

Published online: 11 March 2024

Check for updates

Yuchao Yan[1], Shilong Piao[1,2] ✉, William M. Hammond[3], Anping Chen[4] ✉, Songbai Hong[1], Hao Xu[1], Seth M. Munson[5], Ranga B. Myneni[6] & Craig D. Allen[7]

Vegetation greening has been suggested to be a dominant trend over recent decades, but severe pulses of tree mortality in forests after droughts and heatwaves have also been extensively reported. These observations raise the question of to what extent the observed severe pulses of tree mortality induced by climate could affect overall vegetation greenness across spatial grains and temporal extents. To address this issue, here we analyse three satellite-based datasets of detrended growing-season normalized difference vegetation index ($NDVI_{GS}$) with spatial resolutions ranging from 30 m to 8 km for 1,303 field-documented sites experiencing severe drought- or heat-induced tree-mortality events around the globe. We find that severe tree-mortality events have distinctive but localized imprints on vegetation greenness over annual timescales, which are obscured by broad-scale and long-term greening. Specifically, although anomalies in $NDVI_{GS}$ (ΔNDVI) are negative during tree-mortality years, this reduction diminishes at coarser spatial resolutions (that is, 250 m and 8 km). Notably, tree-mortality-induced reductions in $NDVI_{GS}$ (|ΔNDVI|) at 30-m resolution are negatively related to native plant species richness and forest height, whereas topographic heterogeneity is the major factor affecting ΔNDVI differences across various spatial grain sizes. Over time periods of a decade or longer, greening consistently dominates all spatial resolutions. The findings underscore the fundamental importance of spatio-temporal scales for cohesively understanding the effects of climate change on forest productivity and tree mortality under both gradual and abrupt changes.

Climate change has led to many more extreme events with disastrous consequences on ecosystems and society[1,2]. In particular, increases in the frequency and severity of global drought and heat episodes have caused rising forest stress and extensive pulses of tree mortality[3–7] (Fig. 1a). These pulses of tree mortality can lead to reductions in forest productivity and carbon storage[8–13]. However, at the regional and global scales, greening rather than browning has more often been observed[14–17], frequently leading to enhanced global vegetation

[1]Institute of Carbon Neutrality, Sino-French Institute for Earth System Science, College of Urban and Environmental Sciences, Peking University, Beijing, China. [2]State Key Laboratory of Tibetan Plateau Earth System, Resources and Environment, Institute of Tibetan Plateau Research, Chinese Academy of Sciences, Beijing, China. [3]Institute of Food and Agricultural Sciences, Agronomy Department, University of Florida, Gainesville, FL, USA. [4]Department of Biology and Graduate Degree Program in Ecology, Colorado State University, Fort Collins, CO, USA. [5]U.S. Geological Survey, Southwest Biological Science Center, Flagstaff, AZ, USA. [6]Department of Earth and Environment, Boston University, Boston, MA, USA. [7]Department of Geography and Environmental Studies, University of New Mexico, Albuquerque, NM, USA. ✉e-mail: slpiao@pku.edu.cn; anping.chen@colostate.edu

https://doi.org/10.1038/s41559-024-02372-1

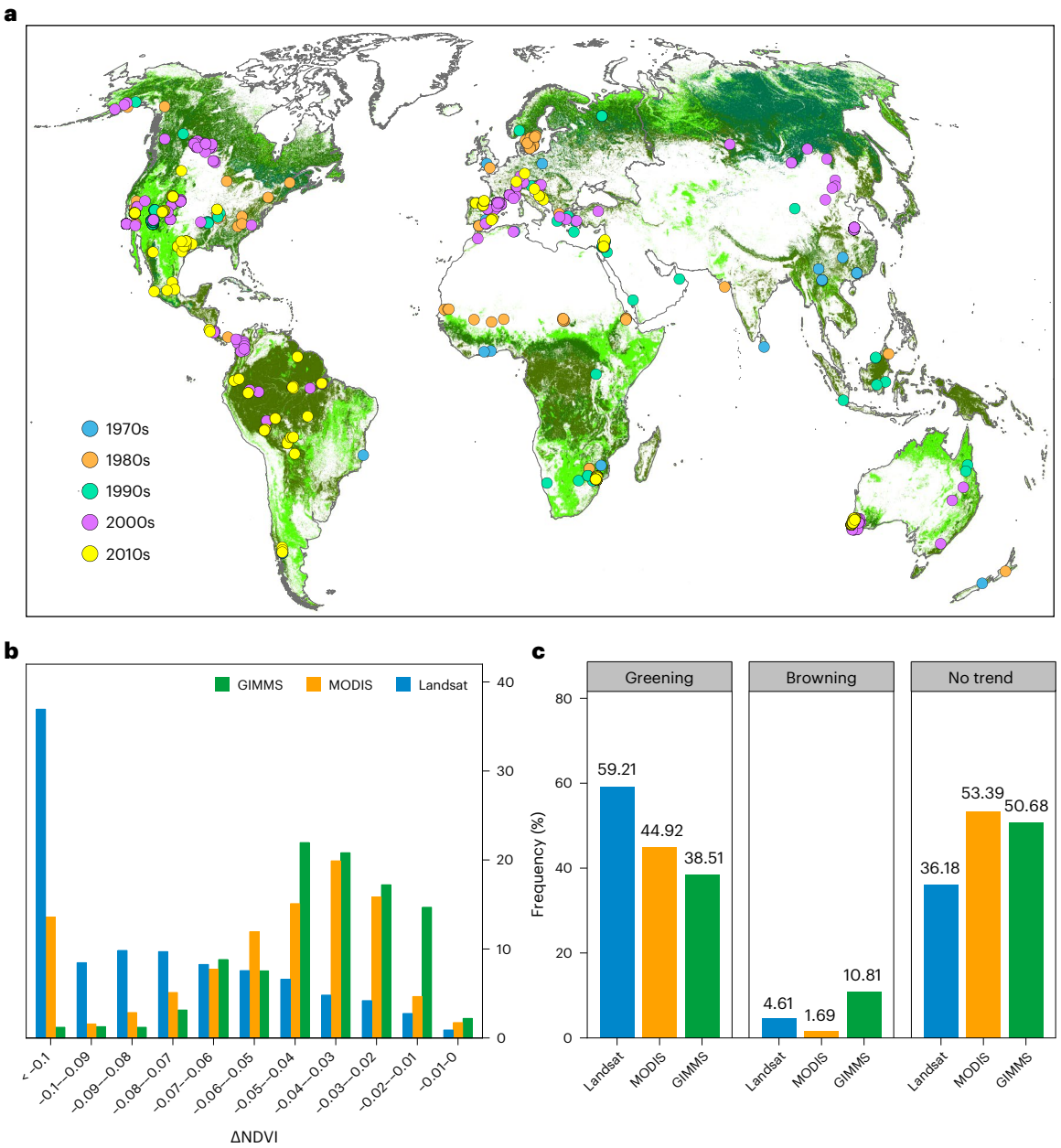

Fig. 1 | Changes in $NDVI_{GS}$ from multiscale sensors corresponding to locations of tree-mortality sites. a, Geographical locations of 1,303 sites across the globe where tree mortality has occurred owing to drought and/or extreme heat since the 1970s (data from a previous study[7]). The background vegetation map shows the distribution of forest (dark green) and shrubland (light green), based on data from the European Space Agency/Climate Change Initiative Land Cover (ESA/CCI-LC) (http://maps.elie.ucl.ac.be/CCI/viewer/). The world continental boundaries were derived from https://hub.arcgis.com/datasets/esri::world-continents/about. **b**, Frequency distributions of $NDVI_{GS}$ anomaly (ΔNDVI) in the occurrence years of tree-mortality events, calculated from detrended $NDVI_{GS}$ time series of the three sensors. **c**, Global fraction of positive (greening), negative (browning), and nonsignificant trends in $NDVI_{GS}$ from Landsat (1984–2020), MODIS (2000–2020) and GIMMS (1982–2015), for locations of tree-mortality sites. Greening (or browning) trends were identified using Mann–Kendall trend analyses at the $P < 0.05$ level (two-sided test).

productivity and carbon storage in terrestrial ecosystems[1,18]. These contrasting observations raise the question of to what extent the detected severe pulses of tree mortality have affected the overall vegetation greenness across temporal and spatial scales. Addressing this question is key for a better understanding of current ecosystem dynamics and long-term trends under the influences of both gradual (for example, warming and CO_2 increase) and abrupt (for example, drought and heatwaves) global change factors, and to realistically forecast the responses of forests to ongoing and projected climate change.

Furthermore, environmental and ecosystem heterogeneity has been suggested to have a crucial role in stabilizing ecosystems under the influence of climatic variations[19,20]. But attempts to quantify the stabilization effect of heterogeneity under extreme climate events on the global scale are still rare, owing largely to the lack of a precisely georeferenced global dataset of extreme climate impacts on ecosystems.

Here we aimed to fill these crucial knowledge gaps by applying remote-sensing time-series observations to field-documented forest tree die-off events, using a dataset of 1,303 precisely georeferenced forest sites where drought- or heat-induced tree mortality had been documented in the scientific literature from 1970–2018 (ref. 7) (Fig. 1a). These sites spanned all major forest types and climate zones on all continents except for Antarctica. We hypothesized that (1) the

effect of documented tree-mortality events on vegetation greenness would be patchy and detectable at fine spatio-temporal resolutions, but would be obscured by an overall greening trend at coarse spatial and temporal resolutions; and (2) this effect of severe climate-induced tree-mortality events could be further mitigated by environmental and ecosystem heterogeneities (for example, topography heterogeneity, forest structure and species diversity), resulting in larger cross-scale differences in vegetation greenness responses for more heterogeneous systems.

To test these hypotheses, we compared the variation in the growing-season normalized difference vegetation index ($NDVI_{GS}$) (refs. 21–23) for 1,303 georeferenced sites across different temporal and spatial scales. For each of these sites, we calculated its $NDVI_{GS}$ for each year from three commonly used satellite sensors that constitute a fine-to-coarse sequence in spatial resolution: Landsat (30 m); the Moderate Resolution Imaging Spectroradiometer (MODIS, 250 m); and the Advanced Very-High-Resolution Radiometer (AVHRR, 8 km, Global Inventory Modeling and Mapping Studies (GIMMS) products) (see Methods). Using these $NDVI_{GS}$ time series, we then compared their differences across spatial scales and between long-term (decades) trends and short-term (years) $NDVI_{GS}$ responses for each combination of site and tree-mortality event. Furthermore, because we expected to see variations in $NDVI_{GS}$ responses to mortality events across different temporal and spatial scales, we also used machine-learning algorithms to determine major environmental and ecosystem factors that help to explain these variations (see Methods). To verify the robustness of our findings, we also conducted a series of validation analyses using different datasets and methods, including the reconstruction of combined grids using Landsat data only; the use of the annual maximum NDVI ($NDVI_{max}$) in place of the fixed growing-season NDVI; and the use of the growing-season enhanced vegetation index (EVI_{GS}) in place of $NDVI_{GS}$ (see Methods).

Results and discussion

$NDVI_{GS}$ responses to tree mortality at different timescales

We found negative anomalies of detrended $NDVI_{GS}$ (ΔNDVI) in the occurrence years of field-documented tree-mortality events across all the sites with all three satellite products (Fig. 1b). This finding indicates that tree-mortality events indeed caused decreases in $NDVI_{GS}$ in the short term. However, when the timescale of the analysis shifted from a few years (that is, the years of and immediately following the mortality event documented in the literature, most of which were shorter than five years) to a decade or longer, we found significant greening trends of long-term $NDVI_{GS}$ time series consistently among the three remote-sensing products of different resolutions for a large proportion (Landsat, 59.21%; MODIS, 44.92%; GIMMS, 38.51%) of these mortality-affected sites (Fig. 1c, Mann–Kendall test, $P < 0.05$). The results suggest that vegetation greening dominates long-term signals even at places that have episodically experienced major tree-mortality events. Furthermore, if the sites were grouped according to the decade in which tree mortality occurred, these long-term greening trends were also consistently observed across different groups (Supplementary Fig. 1)—except for GIMMS $NDVI_{GS}$ during the 2010s, when there were more sites showing browning compared with greening (Supplementary Fig. 1d). Note that the time series of GIMMS $NDVI_{GS}$ in the 2010s was only five years, which might be insufficient for the greening signal to re-emerge. This limitation, together with differences in sensor characteristics and data-processing techniques, helps to explain the higher proportion of sites showing a statistically significant overall browning trend during the entire study period with GIMMS (10.81%; 1982–2015) than with Landsat (4.61%; 1984–2020) or MODIS (1.69%; 2000–2020) time series (Fig. 1c). Together, these results indicate that long-term trends of vegetation greening can obscure intermittent disturbances like tree-mortality events, confirming our first hypothesis from the temporal-scale perspective.

$NDVI_{GS}$ responses at different spatial resolutions

Notably, we also found large discrepancies in the magnitude of $NDVI_{GS}$ decrease during the occurrence years of tree-mortality events across the three different satellite products (Fig. 1b). Specifically, the decrease in $NDVI_{GS}$ was larger than 0.05 (ΔNDVI < −0.05) for more than 80% of the sites with the finer-resolution Landsat dataset (30 m). However, the same large $NDVI_{GS}$ decrease (ΔNDVI < −0.05) was only observed for about 42.79% and 23.15% of the sites with coarser MODIS (250 m) and GIMMS (8 km) products, respectively. Consistent results were also observed using different thresholds (−0.04, −0.06 and −0.07; Supplementary Table 1). The mortality-related ΔNDVI of Landsat was significantly greater than that of the other two products ($P < 0.001$, one-way analysis of variance (ANOVA)). Averaged across the sites, Landsat ΔNDVI (−0.0924) was about 1.56 times MODIS ΔNDVI (−0.0592), and 2.36 times GIMMS ΔNDVI (−0.0391). Considering that the three products covered different time periods, we further compared ΔNDVI for each pair of the products during their overlapping period (Supplementary Fig. 2), and the results again confirmed the finding of a larger decrease in $NDVI_{GS}$ with finer-resolution products. Therefore, tree-mortality events seem to be mostly patchy in nature, with mortality-impaired NDVI signals often diluted and even overshadowed at coarser spatial scales. These confirm our first hypothesis from the spatial-scale perspective.

On the basis of how $NDVI_{GS}$ changed across the multiscale sensors, we divided these sites of ground-observed severe tree mortality into four categories: (1) $NDVI_{GS}$ decreased sharply (ΔNDVI < −0.05) across all the satellite products; (2) $NDVI_{GS}$ decreased sharply according to Landsat and MODIS but slightly (−0.05 < ΔNDVI < 0) according to GIMMS; (3) $NDVI_{GS}$ decreased sharply according to Landsat but slightly according to MODIS and GIMMS; and (4) $NDVI_{GS}$ decreased slightly across all the satellite products (Fig. 2; see Supplementary Table 2 for details). We used digitized Google Earth sub-metre high-resolution satellite images for example sites of the four categories (Supplementary Fig. 3) to illustrate the validity of the classification. For instance, for a site in category 1, we found that the area of tree mortality obtained by manual visual interpretation accounted for 96.23%, 96.2% or 84.44% of the area of a 30 m × 30 m, 250 m × 250 m or 8 km × 8 km pixel, respectively, all centred at the chosen site (Supplementary Fig. 3a,e,i). For a category 2 site, the area of tree mortality accounted for 100% or 84.28% of the area of a 30 m × 30 m or 250 m × 250 m pixel, respectively, but accounted for only 17.55% of the area of an 8 km × 8 km pixel (Supplementary Fig. 3b,f,j). In other words, these categories indicate to what spatial extent the tree mortality of a site is confined (and observed). It is noteworthy that the categories did not show a clear spatial pattern (Fig. 2a–d) and category 1 accounted for only 18.6% of all the sites. This result suggests that only a small percentage of tree-mortality events occurred near-uniformly at broad spatial scales, further confirming that most tree-mortality events are patchy at spatial scales greater than or equal to pixel sizes of 250 m.

Factors determining ΔNDVI differences across spatial scales

We then examined factors that affect tree mortality using a combination of extreme gradient boosting (XGBoost) and Shapley additive explanations (SHAP) models[24,25], and considered 15 factors that are associated with vegetation, topography, soil and climate (see Methods). Here the intensity of tree mortality was approximated with ΔNDVI. At the 30-m resolution, where the mortality-induced $NDVI_{GS}$ decrease was most significant, we found that vegetation-associated factors—of which native plant species richness (NSR) and forest height were the two most important variables—contributed the most in explaining $|\Delta NDVI_{Landsat}|$ (Fig. 3a), the absolute value of ΔNDVI based on Landsat data, which measures the magnitude of $NDVI_{GS}$ decrease induced by tree-mortality events. The SHAP value analysis suggested that higher NSR and taller community canopy height were associated with a smaller decrease in Landsat ΔNDVI (Fig. 3b,c), providing empirical support for the hypothesis that more diverse[26,27] and taller[28–30] forest communities

https://doi.org/10.1038/s41559-024-02372-1

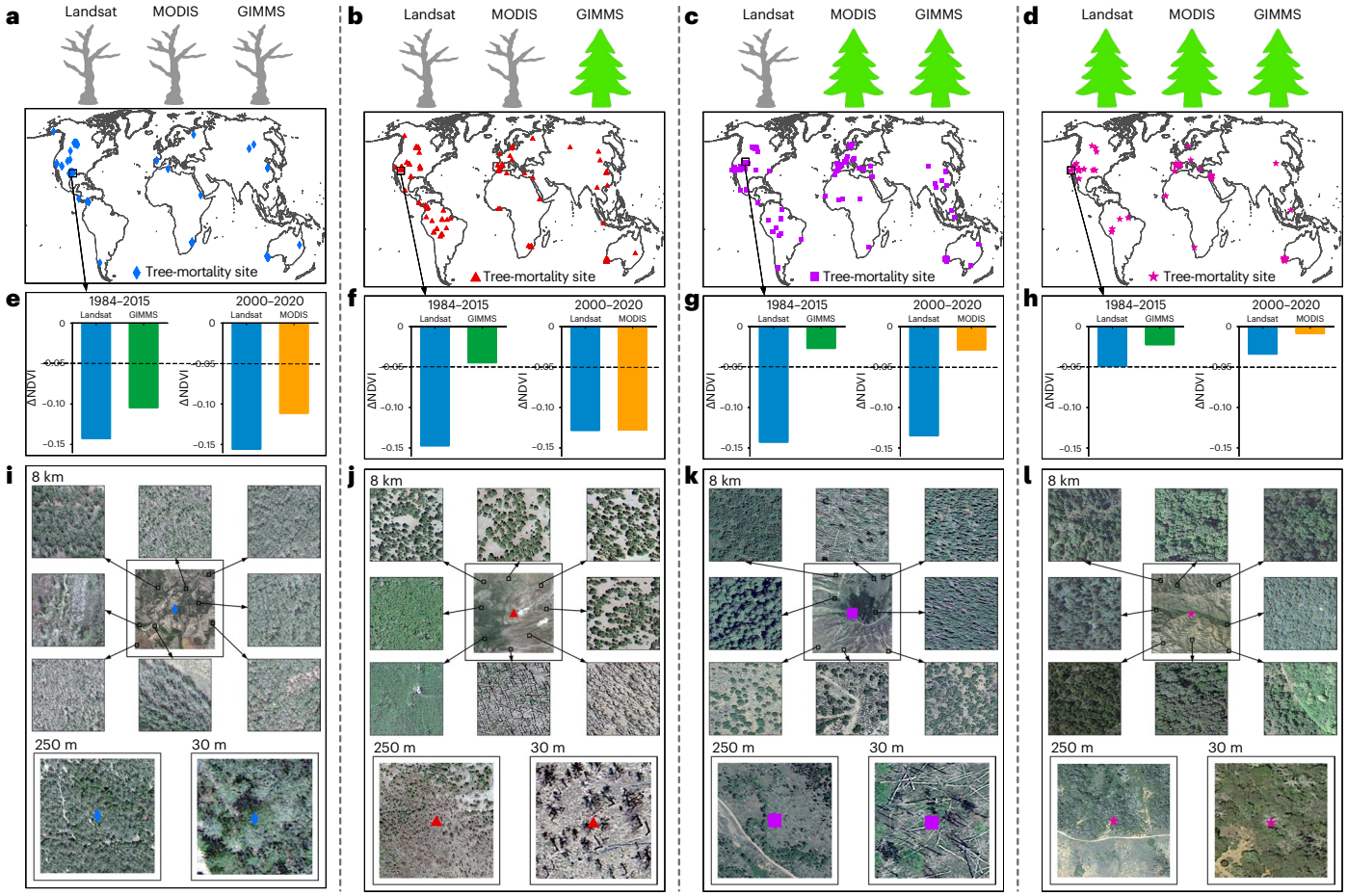

Fig. 2 | Four categories of tree-mortality sites based on ΔNDVI values across different sensors. a–**d**, Spatial distributions of the mortality sites classified into four categories (1–4), on the basis of the criteria listed in Supplementary Table 2. The world continental boundaries were derived from https://hub.arcgis.com/datasets/esri::world-continents/about. **e**–**h**, ΔNDVI from multiscale sensors for four example sites selected from the corresponding category. The example sites from categories 1–4 are located at 96.29080833° W, 30.4684708° N; 111.6126203° W, 35.36789751° N; 109.3074647° W, 41.08904699° N; and 119.7935082° W, 34.01310507° N, respectively. **i**–**l**, The Google Earth sub-metre high-resolution satellite images (0.11–0.13 m) for example sites within windows of 8 km, 250 m and 30 m, respectively. These satellite images were generated during the growing season of the corresponding tree-mortality year (2011, 2011, 2012 and 2013) recorded at the four example sites, respectively. The 8-km window is partially displayed by eight smaller windows around it. Most of the trees inside the 8-km window in **i** have greyish-white canopies and exposed dead trunks. In **j**, the trees with exposed dead trunks are concentrated in the middle and south of the 8-km window. In **k**, the trees with greyish-white canopies and exposed dead trunks show a patchy distribution in the central and northern part of the 8-km window. In the middle and west of the 8-km window in **l**, the trees with greyish-white canopies and exposed dead trunks are also patchy. These features can be observed more clearly on Google Earth by using the latitude and longitude of the example sites and the recorded year of tree mortality. The 250-m and 30-m windows surrounding the example sites also partially display the 8-km window. The areas with tree mortality were visually interpreted manually, on the basis of observed greyish-white canopies and exposed dead trunks (Supplementary Fig. 3).

are more resistant to severe disturbances. It is noteworthy that this evidence was based on field observations of natural tree-mortality events on a global scale, which currently remain inadequately documented in the literature.

Scaling up from the 30-m resolution Landsat data to coarser MODIS and GIMMS products, we found that the differences between the coarser MODIS ΔNDVI and GIMMS ΔNDVI compared with the Landsat ΔNDVI (that is, $Y_{\text{Landsat-MODIS}}$ and $Y_{\text{Landsat-GIMMS}}$; see Methods) were dominated by topographic factors (44.29% and 44.27%, respectively), of which the variable coefficient of elevation (elevation_cv) was most important (Fig. 3d,g). Specifically, a higher elevation_cv corresponded to larger $Y_{\text{Landsat-MODIS}}$ and $Y_{\text{Landsat-GIMMS}}$ (Fig. 3f,h), suggesting that more complex terrain could confine tree mortality to finer scales. More complex terrain, together with fine-scale spatial heterogeneity in topoclimatic and hydrological variations, provides 'microrefugia' (that is, safe islands)[31–35] for forest trees during extreme drought, and thus is more likely to sustain the stability of forest ecosystems at broad scales[36–38]. Nonetheless, an alternative possibility could be the increasing challenge of detecting fine-scale tree-mortality events with coarse-resolution satellite imagery in regions that have high topographic variation. In addition to topographic factors, vegetation factors, including forest canopy height and NSR, were also important variables for explaining the variations in $Y_{\text{Landsat-MODIS}}$ and $Y_{\text{Landsat-GIMMS}}$ (Fig. 3d,g). Both taller forests and higher NSR were more likely to have a larger difference in ΔNDVI between fine and coarse scales (Fig. 3e,i). Photosynthesis in taller Amazon forests, for example, is suggested to be less sensitive to precipitation deficit because the deeper roots of taller trees can access deeper soil moisture when they are suffering from water stress[28]. This could explain why taller trees are able to sustain their growth during drought. Thus, taller forest communities might have more spatial stabilization capacity against fine-scale mortality events. However, we notice that our analyses are at the community level and above, which should not be confused with the mortality resistance of individual trees. That is,

https://doi.org/10.1038/s41559-024-02372-1

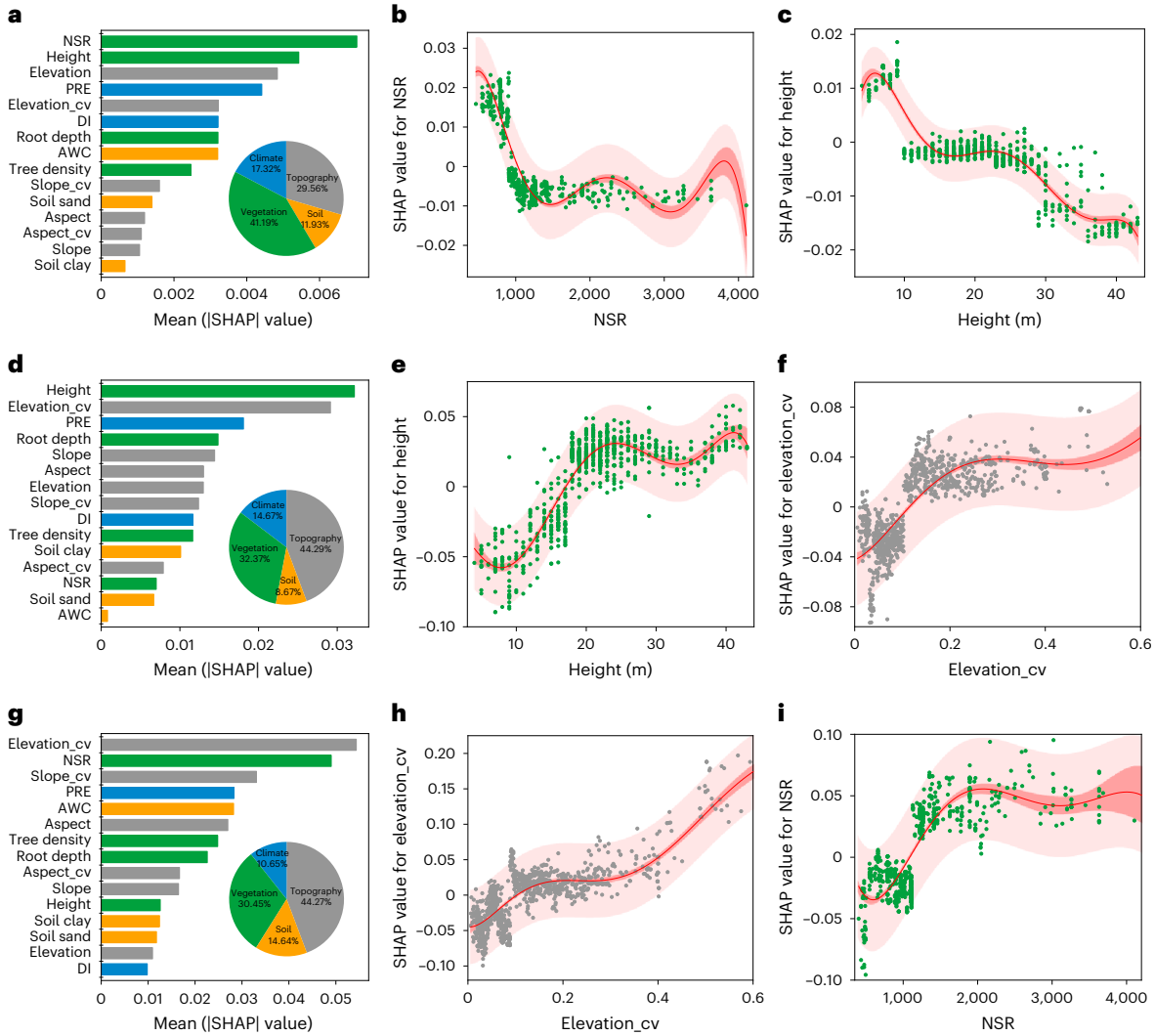

Fig. 3 | Dependence of ΔNDVI from multiscale sensors on potential drivers. **a**,**d**,**g**, The importance of driving factors, in descending order, for variations of $|\Delta NDVI_{Landsat}|$, $Y_{Landsat\text{-}MODIS}$ and $Y_{Landsat\text{-}GIMMS}$, respectively (see Methods). The variable importance is assessed with its mean |SHAP| value (see Methods). Inset pie charts represent the fractional contributions of vegetation, topographic, soil and climate factors. **b**,**c**, Partial dependence plots of the SHAP value against the two most important variables in **a**. **e**,**f**, As for **b**,**c**, but for the two most important variables in **d**. **h**,**i**, As for **b**,**c**, but for the two most important variables in **g**. SHAP > 0 means that the corresponding driver positively affects the dependent variable, and vice versa. The deep pink line represents the fitted line, which provides an approximation of the central tendency or average value of the data points. The deep pink shadings represent the 95% confidence interval of the mean estimate, indicating the range within which we have 95% confidence that the true population mean lies. The light pink shadings represent the 95% prediction interval, indicating that we expect 95% of observations to fall within this interval. PRE, multi-year average precipitation; AWC, available water capacity; DI, drought intensity; slope_cv, inter-pixel variability of slope; aspect_cv, inter-pixel variability of aspect.

forest height here should be viewed as a proxy of forest landscape vertical structural diversity—and more diverse (in the sense of vertical structure) forest landscapes are more resistant to mortality-induced reductions in vegetation greenness. Similarly, higher NSR also provides crucial stabilization mechanisms, for instance, by involving higher diversity in functional traits such as root stratification[39] and differential stomatal regulation strategies[40]. These mechanisms allow plants in a more diverse community to occupy different ecological niches[41,42], increase the asynchronous growth dynamics of different species[43–45] and thus reduce competition for water among species during drought[26,27,41]. Hence, our analyses of factors associated with the cross-scale differences in ΔNDVI during fatal drought events also highlight the essential contributions of habitat heterogeneity and biodiversity to the drought resistance of vegetation greenness (that is, resistance to the spread of the drought-induced reduction in vegetation greenness).

Verification of results with different methods and datasets

Many factors could influence our observed results, including systematic differences, varied spatio-temporal coverages, the resolution of sensors, growing-season categories, vegetation index and the selection of climate datasets, as well as spatial autocorrelation between mortality sites. To assess whether these factors might have biased or even jeopardized the robustness of our findings, we performed a series of verification analyses.

To test whether the observed discrepancies of ΔNDVI between different satellite products are indeed caused by their different spatial resolutions rather than by systematic differences among sensors, we used Landsat $NDVI_{GS}$ to construct combined grids of 270 m (a combined grid of 9 × 9 Landsat pixels, which is close to the 250-m resolution of a MODIS pixel) and about 8 km (a combined grid of 267 × 267 Landsat pixels, which is close to the 8-km resolution of a GIMMS pixel), respectively, centring on the tree-mortality site (Fig. 4a and Supplementary

https://doi.org/10.1038/s41559-024-02372-1

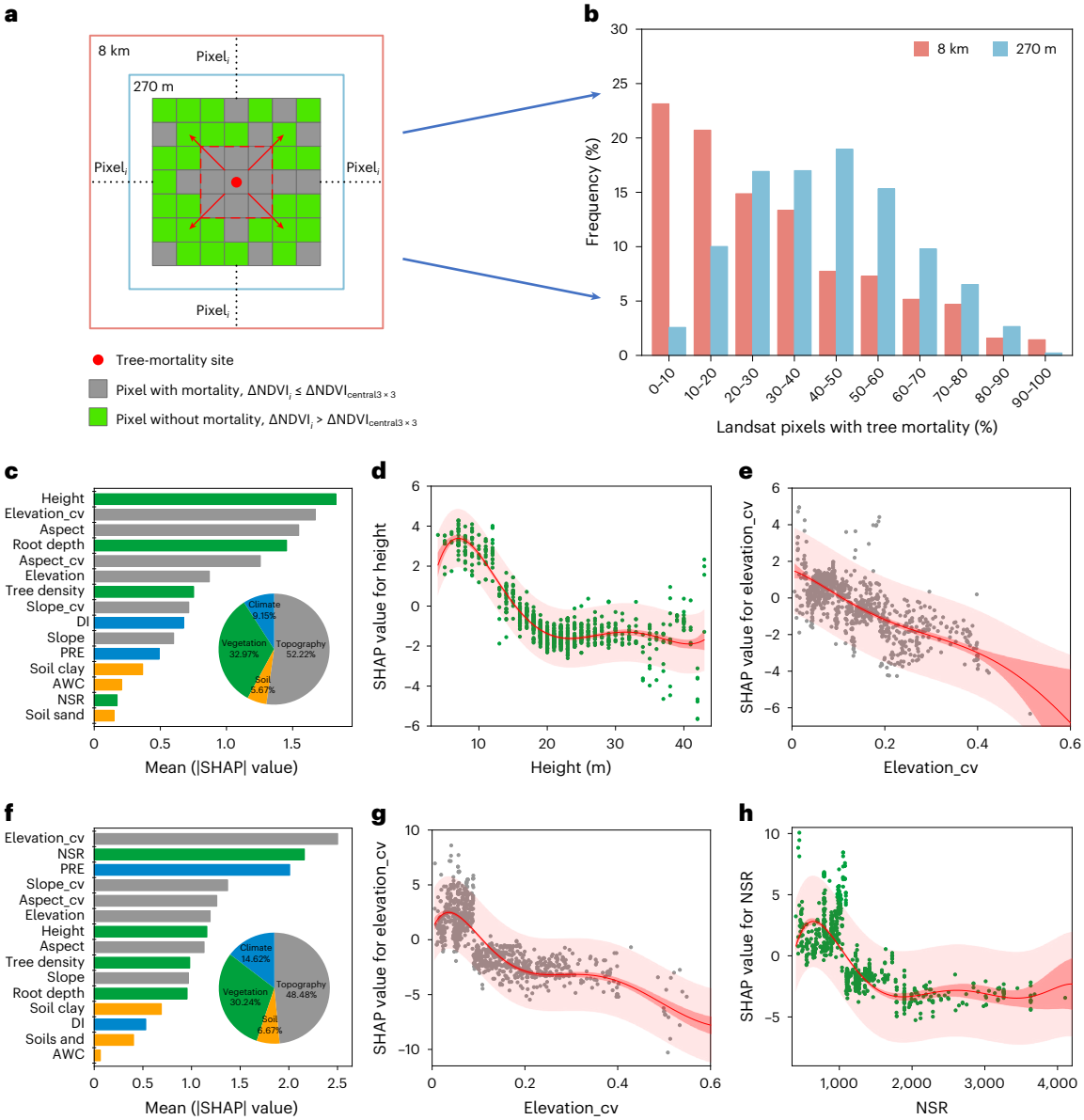

Fig. 4 | Percentage of Landsat pixels with tree mortality within 270-m ($P_{270\ m}$) and 8-km ($P_{8\ km}$) combined grids and its drivers. a, Schematic diagram showing how to estimate the fraction of Landsat pixels with tree mortality within a 270-m or 8-km combined grid. Landsat pixels impaired by tree mortality are identified as those in which the corresponding ΔNDVI is no greater than the average ΔNDVI of the 3 × 3 pixels centring on the tree-mortality site (that is, $\Delta NDVI_{central3\times3}$, in the red dotted box), whereas Landsat pixels without tree mortality are considered as those characterized by $\Delta NDVI > \Delta NDVI_{central3\times3}$. **b**, Frequency distributions of $P_{270\ m}$ and $P_{8\ km}$ across tree-mortality sites. **c**,**f**, The importance of driving factors, in descending order, for the spatial variations of $P_{270\ m}$ and $P_{8\ km}$, respectively (see Methods). The variable importance is assessed with its mean |SHAP| value (see Methods). Inset pie charts represent the fractional contributions of vegetation, topographic, soil and climate factors. **d**,**e** and **g**,**h** are the partial dependence plots of the SHAP value against the two most important variables in **c** and **f**, respectively. SHAP > 0 means that the corresponding driver positively affects the dependent variable, and vice versa. The deep pink line represents the best-fit line, which provides an approximation of the central tendency or average value of the data points. The deep pink shadings represent the 95% confidence interval of the mean estimate, indicating the range within which we have 95% confidence that the true population mean lies. The light pink shadings represent the 95% prediction interval, indicating that we expect 95% of observations to fall within this interval. Abbreviations as in Fig. 3.

Fig. 4a; see Methods). We found that the central 3 × 3 pixels within the combined grid (that is, the 3 × 3 pixels centring on the tree-mortality site) had significantly stronger negative anomalies of detrended $NDVI_{GS}$ during mortality years than did the surrounding non-central pixels (probably having less severe mortality or with no mortality) (Supplementary Fig. 4b, $P < 0.001$, one-way ANOVA), whereas the long-term increasing trends in the central 3 × 3 pixels were significantly weaker than those in the surrounding non-central pixels (Supplementary Fig. 4c). Therefore, we assumed that the central 3 × 3 pixels within each combined grid was the core area in which severe tree mortality occurred, and the average ΔNDVI in the core area (that is, $\Delta NDVI_{central3\times3}$) was used as the baseline for identifying pixels with tree mortality. A pixel (30-m resolution) was viewed as impaired by tree mortality if its $\Delta NDVI \le \Delta NDVI_{central3\times3}$; otherwise, it was free from tree-mortality effects. We then calculated the percentages of Landsat pixels impaired by tree mortality within each 270-m ($P_{270\ m}$) or 8-km ($P_{8\ km}$) combined grid for the corresponding tree-mortality site.

As shown in Fig. 4b, the frequency histogram of $P_{270\ m}$ and $P_{8\ km}$ peaked in 40–50% and 0–10%, respectively. Most of the mortality sites (65.48% and 79.82%, respectively) had a $P_{270\ m}$ or $P_{8\ km}$ value lower than

50%, and only 19.20% (12.90%) of the sites had a $P_{270\,m}$ ($P_{8\,km}$) value higher than 60%. Therefore, we again confirmed that most of the tree-mortality events are patchy and often spatially dispersed within and between field sites. This patchy nature means that over progressively larger scales of inquiry, extensive tree-mortality events may become harder to detect and thus are underestimated by coarser-resolution sensors.

Consistent with the analyses on $Y_{Landsat\text{-}MODIS}$ and $Y_{Landsat\text{-}GIMMS}$ (Fig. 3d,g), we also found that topographic factors—in particular, the elevation_cv—dominated the variations of $P_{270\,m}$ and $P_{8\,km}$ (52.22% and 48.48%; Fig. 4c,f) with the same XGBoost and SHAP models. A higher elevation_cv corresponded to lower $P_{270\,m}$ and $P_{8\,km}$ values (Fig. 4e,g). Similarly, vegetation factors such as forest height and NSR also had significant roles in controlling $P_{270\,m}$ and $P_{8\,km}$ (Fig. 4c,f), whereby taller forests and greater NSR were associated with lower $P_{270\,m}$ and $P_{8\,km}$ values (Fig. 4d,h). These results further confirmed our findings based on direct comparisons of ΔNDVI at different scales, and again emphasized the importance of habitat heterogeneity and biodiversity to the drought resistance of vegetation greenness.

We also conducted the following verifications to test whether spatio-temporal differences in coverage between sensors could confuse the results. First, we compared the trends in $NDVI_{GS}$ with different satellite products in their overlapping time periods (the overlapping period between Landsat and GIMMS: 1984–2015; between Landsat and MODIS: 2000–2020; and among Landsat, MODIS and GIMMS: 2000–2015) (Supplementary Fig. 5). The results confirmed that there were more tree-mortality sites showing greening than there were showing browning trends, especially at longer timescales such as 1984–2015 and 2000–2020 (Supplementary Fig. 5a,b). Second, we compared different sensors in windows of roughly the same size. To do this, we used combined Landsat grids of 270 m and 8 km, which were compared to the similarly sized MODIS and GIMMS pixels, respectively. As shown in Supplementary Fig. 6, the results based on Landsat data still showed generally more negative ΔNDVI than did those based on GIMMS and MODIS, confirming that mortality events are often spatially quite patchy and can be better captured by finer-resolution sensors.

We also used different vegetation indices and climate data to verify the results. For example, using $NDVI_{max}$ and EVI_{GS}, we obtained results that were consistent with those based on $NDVI_{GS}$ (Supplementary Figs. 7 and 8). We also used precipitation and the standardized precipitation–evapotranspiration index (SPEI) with a spatial resolution of 0.5° in place of precipitation and the Palmer drought severity index (PDSI) in the TerraClimate database with a spatial resolution of 4 km, and reran the XGBoost and SHAP models. As shown in Supplementary Fig. 9, the dominant factors explaining variation are consistent with those based on TerraClimate, suggesting that the choice and resolution of climate data did not confound our findings. Finally, to overcome the problem that some tree-mortality sites might occur in a same pixel (especially for coarse MODIS and GIMMS datasets), and the issue of spatial autocorrelation, we conducted two types of additional analyses. First, when two or more sites co-occur in the same GIMMS or MODIS pixel, we randomly selected one tree-mortality site within each of these pixels to compare the difference between the coarser MODIS-derived (or GIMMS-derived) ΔNDVI and the Landsat-derived ΔNDVI. We then also reran the XGBoost and SHAP models with only one site from each pixel. We still obtained similar results, including the generally lower ΔNDVI with Landsat than with GIMMS and MODIS (Supplementary Fig. 10), and the dominant factors explaining $Y_{Landsat\text{-}MODIS}$ and $Y_{Landsat\text{-}GIMMS}$ with the machine-learning model (Supplementary Fig. 11). Second, we aggregated the dependent and independent variables of these sites to a common grid (250 m, 500 m and 1,000 m) (see Methods), and then reran the XGBoost and SHAP models. As shown in Supplementary Fig. 12, the dominant factors explaining variation based on the aggregation data are still consistent with those based on the original data.

There are a few caveats and possible limitations of our analysis that need to be noted. First, the recovery in $NDVI_{GS}$ could be due to the growth of non-forest components (for example, shrubs or herbaceous plants) or much younger forests, which might not provide the same ecosystem services or productivity, structural characteristics or carbon storage as pre-mortality forests, even with the same NDVI values. Hence, our greenness-based findings should be interpreted with caution, and they do not necessarily imply that ecosystem function is resistant to or can fully recover from climate-induced mortality events.

It is also crucial to acknowledge potential limitations of our machine-learning analyses, as a result of the variations in spatial resolution among data sources. In particular, the data for climate, soil and vegetation attributes all have a relatively coarse spatial resolution, which makes it challenging to accurately capture fine-scale variations within individual grid cells. However, it is worth noting that we partially addressed this limitation by incorporating topography heterogeneity represented by digital elevation model (DEM) data at 30-metre resolution. This high-resolution proxy could partially capture the within-grid variations in climate, soil and vegetation attributes for the topographical influences on microclimatic conditions and soil properties[46]. The proxy role of topographical heterogeneity for some aspects of climate, soil and vegetation attributes could provide valuable insights into cross-scale ΔNDVI relationships, including the role of fine-scale habitat variations in modulating the responses of vegetation greenness and its potential underlying ecosystem processes to severe climate-induced mortality events. Nevertheless, topography data alone may still be insufficient to fully capture the direct effects of climate soil and vegetation attributes. Future research should investigate possible synergistic effects by incorporating higher-resolution data for climate, soil and vegetation attributes, and topography, to gain a more comprehensive understanding of the mechanisms that underlie the responses of vegetation to severe climate disasters across spatial and temporal scales.

Summary

Through a comparison of remotely sensed vegetation greening and browning trends at different spatio-temporal scales across 1,303 tree-mortality sites, we have shown that seemingly contrasting observations—global vegetation greening versus increasing tree mortality—generally manifest at different temporal and spatial scales. Severe tree-mortality events have short-term negative effects on remote-sensing-derived vegetation greenness at a fine spatial resolution. These effects, however, can be partly or even entirely obscured when examined at coarser spatial scales or over longer timescales. Our findings highlight the key roles of topographic heterogeneity and species richness in confining the impact of tree-mortality events to fine scales. This underscores the importance of preserving habitat heterogeneity and biodiversity to enhance the resistance of ecosystems to climate extremes on broad scales. Furthermore, it is worth noting that current dynamic global vegetation models which typically operate at coarse spatial grains[18,47] (for example, 0.5°) and often neglect within-grid spatial heterogeneity, may underestimate or even overlook mortality-induced carbon loss at finer spatial scales. However, it is also essential to recognize that the recovery of $NDVI_{GS}$ after tree-mortality events does not necessarily imply a return to the pre-mortality state in terms of forest structure and functioning[48,49]. Thus, relying solely on the greening trend does not provide a comprehensive understanding of post-mortality forest recovery. Our study also highlights the necessity for high spatial resolutions (for example, 30 m or finer) of field-based observational data and more realistic, process-based model simulations of vegetation growth and dieback. These are urgently needed to enable us to gain a better understanding of—and to more accurately predict—ecosystem dynamics and their carbon-cycle consequences under current and future climate change.

Methods

Tree-mortality sites

The global dataset of tree-mortality sites used in this study was obtained from a meta-analysis of previously reported tree-mortality events[7]. This dataset records the georeferenced locations of 1,303 sites that document the timing of tree-mortality events resulting from extreme drought and heat stress from 1970–2018, which were collected from 154 peer-reviewed studies. These sites encompass a wide range of forest types and climate zones across all continents except Antarctica. Detailed information about the dataset can be found in a previous report[7], and at https://www.iufro.org/science/task-forces/tree-mortality-patterns. Because these 1,303 sites were from published studies that included on-the-ground assessments of tree mortality and climatic association with hotter drought stress, they are not spatially representative of all mortality events, and like most published field data, show a bias for the northern hemisphere, and for drier field sites (for more details, see ref. 7). Note that only 27 sites involved mortality events before 1982 and hence cannot be used to explore mortality-induced negative anomalies in NDVI. However, these few data points still provide supporting evidence of decadal-scale vegetation greening trends, even when their immediate responses to tree-mortality events cannot be captured by satellite imagery.

NDVI and EVI datasets

NDVI and EVI are widely used remote-sensing proxies to detect changes in terrestrial vegetation activity[15,16], including the responses to drought and/or heat stress[50]. The NDVI and EVI datasets from different satellite sensors (AVHRR, MODIS and Landsat) and with different spatio-temporal resolutions were included in our analysis. Detailed information about the three NDVI and EVI products is provided below.

We obtained the AVHRR-based NDVI data from Global Inventory Modeling and Mapping Studies version 3 (GIMMS 3g; https://poles.tpdc.ac.cn/en/data/9775f2b4-7370-4e5e-a537-3482c9a83d88/). This product is available at a spatial resolution of 1/12° (about 8 km) and a temporal resolution of 15 days from 1982 to 2015 (ref. 51). MODIS NDVI and EVI are derived from the Collection 6 vegetation indices product MOD13Q1 with a spatial resolution of 250 m and a temporal resolution of 16 days between 2000 and 2020, which is computed from atmospherically corrected bidirectional surface reflectance. We aggregated biweekly NDVI and EVI values to monthly using the maximum value composite method to eliminate the contamination from cloud, atmosphere and changes in solar altitude angle[52]. In our study, we averaged the monthly NDVI values from the GIMMS dataset and the monthly NDVI and EVI values from the MODIS dataset over the entire growing season. The growing season was considered as April–October for landmass north of 23.5° N, October–April for south of 23.5° S, and year-round for between 23.5° N and 23.5° S (refs. 21–23).

The Landsat retrievals with a spatial resolution of 30 m and temporal resolution of 16 days are ideally suited for regional- to global-scale time-series analysis, particularly with the release of higher-level surface reflectance products from Landsat 5 Thematic Mapper (TM), 7 Enhanced Thematic Mapper Plus (ETM+) and 8 Operational Land Imager (OLI) since 1984. Surface reflectance from Landsat 5 and 7 has been atmospherically corrected using the Landsat Ecosystem Disturbance Adaptive Processing System (LEDAPS)[53,54], and that from Landsat 8 has been atmospherically corrected using the Landsat Surface Reflectance Code (LaSRC)[55]. The Landsat surface reflectance products also provide pixel-scale data-quality flag information indicating clear-sky, water, snow, cloud or shadow conditions, as determined by the C Function of Mask (CFMASK) algorithm[56]. We applied the quality flag information to remove the effects of clouds and their shadows in Landsat imagery. In total, 114,786 Landsat surface reflectance images (Collection 1 Tier 1) during the growing season from 1984 to 2020 were used. Surface reflectance images from Landsat 5, Landsat 7 and Landsat 8 were used for the periods of 1984–2011, 1999–2002 and 2012, and 2013–2020, respectively. Landsat 7 images are not available from 31 May 2003, owing to the failure of the Scan Line Corrector (SLC); the gaps of Landsat 7 SLC-off images in 2012 were filled using a focal mean function provided by Google Earth Engine (GEE). We adjusted the surface reflectance products among sensors (that is, Landsat 5 TM, 7 ETM + , and 8 OLI) to be more consistent using ordinary least squares transformation functions[57], and estimated Landsat-based $NDVI_{GS}$ and EVI_{GS}. To avoid systematic errors in site geolocation, we averaged Landsat $NDVI_{GS}$ and EVI_{GS} from a 3 × 3-pixel window centring on each tree-mortality site. Moreover, we also obtained the annual maximum of GIMMS-, MODIS- and Landsat-based NDVI values using the maximum value composite method[52].

Note that owing to the large volumes of Landsat images, the processing of the satellite data was implemented in GEE, a cloud computing platform capable of analysing remote-sensing data on a global scale[58,59]. In this study, the $NDVI_{GS}$, $NDVI_{max}$ and EVI_{GS} values of Landsat and MODIS were acquired and preprocessed through the JavaScript application programming interface in GEE[60].

Climatic datasets

Global gridded monthly precipitation and PDSI product in the TerraClimate database[61], with a spatial resolution of 4 km and covering the period 1970–2020, were provided by GEE (IDAHO_EPSCOR/TERRACLIMATE). Gridded data of the SPEI were obtained from SPEIbase v.2.6 (https://digital.csic.es/handle/10261/202305) with a 0.5° spatial resolution and a monthly temporal resolution from 1901 to 2018 (ref. 62). The SPEI products were produced across a range of timescales from 1 to 48 months. The hydraulic failure and dieback of woody trees often react to drought stress in a time-lagged manner, so SPEI data integrated over 12-month timescales were chosen as an indicator of vegetation water stress in this study[63]. For each tree-mortality event, we calculated the average PDSI and SPEI of the growing season and also recorded the lowest value during the corresponding tree-mortality years, as a measure of drought intensity. We also obtained monthly precipitation data, with a spatial resolution of 0.5° and covering the period 1980–2015, from the Climatic Research Unit (CRU)[64] (https://data.ceda.ac.uk/badc/cru/data/cru_ts). We calculated the multi-year average precipitation patterns during their period. We extracted the PDSI, SPEI and precipitation from the above climatic datasets for the locations of tree-mortality sites.

Soil datasets

Global maps of AWC, soil clay and soil sand, all with a spatial resolution of 0.05°, were downloaded from the Regridded Harmonized World Soil Database v.1.2 (ref. 65) (https://daac.ornl.gov/SOILS/guides/HWSD.html). The AWC identifies seven textural classes representing capacities of 150, 125, 100, 75, 50, 15 and 0 mm water per m of the soil unit, respectively. In general, soil clay has a stronger water retention capacity than does soil sand. We extracted the soil information from gridded data according to the locations of tree-mortality sites.

Datasets of tree attributes

Canopy height was obtained from the Global Forest Canopy Height dataset[66] (https://webmap.ornl.gov/ogc/dataset.jsp?dg_id=10023_1). Global maximum rooting depth was derived from the project of Global Earth Observation for Integrated Water Resource Assessment (Earth2Observe, https://wci.earth2observe.eu/thredds/catalog/usc/root-depth/catalog.html). Tree density was derived from a global product generated from ground-sourced measurements of tree density[67] (https://elischolar.library.yale.edu/yale_fes_data/1/), which is used as a measure of competitive pressure among individual trees. All three datasets have a spatial resolution of 1 km. When the data were used at 30-m and 250-m scales, we directly extracted these tree attributes on the basis of the locations of tree-mortality sites. To be consistent with the data analyses conducted at the 8-km scale, we averaged the original

data for each 8 × 8 grid centred on each tree-mortality site. A global map of NSR composed by equal-area hexagonal grid cells of 7,800 km^2 was downloaded from the Anthroecology Lab[68] (https://anthroecology.org/). We used the locations of tree-mortality sites to extract the NSR values of the corresponding hexagonal grid cell. In this study, owing to the unavailability of realized species richness data, NSR data were used to indirectly indicate the global plant species richness gradient. NSR is a metric that measures the abundance of native plant species in a given region or area, and is often used to compare plant biodiversity across different locations[69]. Although NSR does not directly reflect the actual plant species richness of a particular location or area, it can provide valuable information for studying global plant species richness when actual data are not available.

Topographic datasets

Elevation, slope and aspect were extracted from the Shuttle Radar Topography Mission (SRTM) 30-m-resolution DEM data. We averaged the elevation, slope and aspect values for a 3 × 3-pixel window, 9 × 9-pixel window (270 m × 270 m) and 267 × 267-pixel window (about 8 km × 8 km) centring on each tree-mortality site, for data analyses conducted at 30-m, 250-m and 8-km scales, respectively. We further calculated the inter-pixel variability of elevation (that is, elevation_cv), slope (that is, slope_cv) and aspect (that is, aspect_cv) within the 267 × 267-pixel window, representing the regional terrain complexity surrounding each site. We used the coefficient of variation as a measure representing the ratio of the standard deviation to the mean. The calculations of topographic factors were performed on GEE.

Data analyses

We performed the following analyses to characterize the relationship between tree mortality and greening trends. First, we conducted Mann–Kendall trend analysis to examine the long-term trends of $NDVI_{GS}$, $NDVI_{max}$ and EVI_{GS} at the locations of tree-mortality sites (Fig. 1c and Supplementary Figs. 1, 4c, 5, 7a and 8a,b). The Mann–Kendall test is a non-parametric test method that has been widely used to detect the change trend in satellite-based vegetation index time series[14,17]. In this study, we used the Mann–Kendall trend test modified to account for temporal autocorrelation[70] in the time-series data, and identified significant trends in Mann–Kendall trend analysis at the $P < 0.05$ level.

Second, we calculated ΔNDVI values as a measure of the short-term effect of tree mortality (Fig. 1b). ΔNDVI is the detrended anomaly of $NDVI_{GS}$ in the years of tree-mortality occurrence. Here, after detrending the $NDVI_{GS}$ time-series data, ΔNDVI was calculated as the deviation of $NDVI_{GS}$ during those specific years from its long-term average. This approach allows for the identification and analysis of changes in $NDVI_{GS}$ that can be attributed to tree-mortality events, independent of any long-term trends or variations present in the entire dataset[71]. Furthermore, we compared ΔNDVI among the three satellite products for their entire period using the one-way ANOVA. Considering that the three products covered different time periods, we also conducted paired comparisons on ΔNDVI for each pair of the three products over their overlapping time period using the *t*-test (Supplementary Fig. 2).

Third, by comparing the ΔNDVI values among satellite products with different resolutions, we divided all the available sites into four major categories: (1) $NDVI_{GS}$ decreased sharply ($\Delta NDVI_{GS} < -0.05$) across all products; (2) $NDVI_{GS}$ decreased sharply according to Landsat and MODIS but slightly ($-0.05 < \Delta NDVI_{GS} < 0$) according to GIMMS; (3) $NDVI_{GS}$ decreased sharply according to Landsat but slightly according to MODIS and GIMMS; and (4) $NDVI_{GS}$ decreased slightly across all products (Supplementary Table 2). For each category, an example site of tree mortality was displayed with Google Earth sub-metre-resolution satellite images (Fig. 2). These tree-mortality sites selected for categories 1–4 are located at 96.29080833° W, 30.4684708° N; 111.6126203° W, 35.36789751° N; 109.3074647° W, 41.08904699° N; and 119.7935082° W, 34.01310507° N, respectively. The areas with tree mortality and without tree mortality within the 8-km, 250-m and 30-m windows surrounding the example sites were visually interpreted according to the greyish-white canopies and exposed dead trunks observed on Google Earth (Fig. 2 and Supplementary Fig. 3).

Fourth, to understand the potential factors driving variations in $|\Delta NDVI_{Landsat}|$ (the intensity of tree mortality at a 30-m scale), we used a combination of XGBoost and SHAP models to examine the relationship between $|\Delta NDVI_{Landsat}|$ and 15 independent variables (that is, drought intensity, average annual precipitation, AWC, soil clay content, soil sand content, forest height, root depth, tree density, NSR, elevation, slope, aspect, elevation_cv, slope_cv and aspect_cv) (Fig. 3a–c). XGBoost and SHAP models are widely used in Earth science research[72–76]. XGBoost is an enhanced version of a gradient-boosting decision tree algorithm that has shown superior performance in achieving a fast computation speed and the ability to deal with sparse datasets[77]. XGBoost adopts a stepwise shrinkage process that limits overfitting[77]. SHAP is based on the concept of the Shapley value in game theory[24,25]. SHAP is a unified approach to explain the output of any machine-learning model and to visualize the complex causal relationship between the dependent variable and its driving factors[24,25]. In this study, we used SHAP to describe the non-linear relationships hidden in the black box model of XGBoost and to transform these into interpretable rules, and then explored the impact magnitude and direction (positive or negative) of multiple factors. It is noteworthy that collinearity among independent variables could lead to confounding results in the XGBoost and SHAP models. Therefore, we tested for the multicollinearity among independent variables by calculating the variance inflation factor (VIF) values for each variable, and only included factors with VIF < 10 as model inputs[78]. In addition, for cross-site comparisons, we used temporally static values of independent variables for each site (for example, PRE, soil property, forest height and NSR) to explore how the dependent variable changes along the broad environmental gradients (for example, climate gradients, soil gradients and vegetation gradients) of different independent variables. Hence, here all the independent variables for a given site (for example, PRE is the multi-year average precipitation of a site) should be unchanged for the purpose of spatial analysis.

Fifth, the same machine-learning model was also used to analyse the influence of driving factors on the difference of tree-mortality intensities at different spatial scales (Fig. 3d–i), which was defined as follows:

$$Y_{\text{Landsat-MODIS}} = \frac{|\Delta NDVI_{Landsat} - \Delta NDVI_{MODIS}|}{|\Delta NDVI_{Landsat}|} \quad (1)$$

$$Y_{\text{Landsat-GIMMS}} = \frac{|\Delta NDVI_{Landsat} - \Delta NDVI_{GIMMS}|}{|\Delta NDVI_{Landsat}|} \quad (2)$$

where $Y_{\text{Landsat-Modis}}$ represents the relative difference between Landsat and MODIS ΔNDVI during 2000–2020, and $Y_{\text{Landsat-GIMMS}}$ represents the relative difference between Landsat and GIMMS ΔNDVI during 1984–2015, for each tree-mortality site. $\Delta NDVI_{Landsat}$, $\Delta NDVI_{MODIS}$ and $\Delta NDVI_{GIMMS}$ were calculated in the years of tree-mortality occurrence, based on detrended anomalies of Landsat, MODIS and GIMMS $NDVI_{GS}$ time series, respectively.

Sixth, we performed a series of additional data analyses to test the robustness of our results. (1) To remove potential influences of the systematic differences between sensors and verify the robustness of associated results, we further analysed $NDVI_{GS}$ from Landsat only with constructed combined grids of 270 m (that is, a combined grid of 270 m × 270 m from 9 × 9 Landsat pixels) and about 8 km (that is, a combined grid of 8 km × 8 km from 267 × 267 Landsat pixels), centring on the tree-mortality site (Fig. 4a and Supplementary Fig. 4a). The 270-m and 8-km combined $NDVI_{GS}$ grids for each tree-mortality site from 1984 to 2020 (total 92,746 combined images) were calculated using the Landsat 5, 7 and 8 surface reflectance products in GEE. After detrending Landsat

$NDVI_{GS}$ time series pixel by pixel, we obtained ΔNDVI for each pixel within the 270-m and 8-km combined grids in the years of tree-mortality occurrence (similar methods were used to construct 8-km combined EVI_{GS} girds and calculate ΔEVI; Supplementary Fig. 8). The 3 × 3-pixel window in the centre of the combined grid (that is, the 3 × 3-pixel window centring on the tree-mortality site) was assumed to be the core area of tree-mortality occurrence, and the average ΔNDVI in the core area (that is, $\Delta NDVI_{central3\times3}$) was used as the baseline to identify the pixels with tree mortality within each combined grid. A pixel with $\Delta NDVI \leq \Delta NDVI_{central3\times3}$ was identified to have experienced tree mortality, otherwise it was identified not to have experienced tree mortality (Fig. 4a). Accordingly, we calculated the percentages of Landsat pixels with tree mortality within the 270-m ($P_{270\,m}$) or 8 km ($P_{8\,km}$) combined grids for each tree-mortality site (Fig. 4b). Finally, we used the XGBoost and SHAP models to examine the factors driving the variations in $P_{270\,m}$ (Fig. 4c–e) and $P_{8\,km}$ (Fig. 4f–h). The model performance was evaluated by randomly splitting the dataset into 70% for training and 30% for testing. Using regression analysis of predicted and observed values of the test dataset, the R^2, root mean square error (RMSE), relative root mean square error (RRMSE) and bias were obtained to measure the model accuracy. We repeated this process ten times for each model to avoid the contingency (Supplementary Fig. 13). (2) To make a comparison over the same time period, we compared the trends in $NDVI_{GS}$ during the overlapping time period of different sensors (Supplementary Fig. 5). (3) To make a comparison in windows of the same size, we compared the combined grids of 270 m and 8 km based on the Landsat data (Fig. 4a and Supplementary Fig. 4a), with the corresponding MODIS- and GIMMS-derived ΔNDVI (Supplementary Fig. 6). (4) To test the robustness of $NDVI_{GS}$ results, we analysed the trends in $NDVI_{max}$ and EVI_{GS}, and compared $\Delta NDVI_{max}$ (and ΔEVI) at different resolutions (Supplementary Figs. 7 and 8). (5) To test whether the resolution of the climate data affected our findings, we used precipitation and SPEI at 0.5° resolution in place of precipitation and PDSI at 4-km resolution, and reran the machine-learning model (Supplementary Fig. 9). To address the issues of the different spatial resolution of the datasets and the spatial autocorrelation between mortality sites as much as possible, we randomly selected one tree-mortality site within every coarse pixel (GIMMS or MODIS) to compare the difference between the coarser MODIS-derived (or GIMMS-derived) ΔNDVI and the Landsat-derived ΔNDVI (Supplementary Fig. 10), and then reran the machine-learning model (Supplementary Fig. 11); furthermore, we aggregated the average of the dependent variables and independent variables of these sites at a common grid (250 m, 500 m and 1,000 m), and then reran the machine-learning model. That is, when more than one site was located in the same grid (250 m, 500 m and 1,000 m), we calculated the average value of these sites and used it as input for the machine-learning model (Supplementary Fig. 12).

Reporting summary

Further information on research design is available in the Nature Portfolio Reporting Summary linked to this article.

Data availability

The tree-mortality sites can be found at https://www.iufro.org/science/task-forces/tree-mortality-patterns (https://doi.org/10.6084/m9.figshare.24847698) (ref. 79). The Google Earth submetre high-resolution satellite images can be found at https://doi.org/10.6084/m9.figshare.23243915 (ref. 80). The climate, vegetation and soil data can be found at https://doi.org/10.6084/m9.figshare.24847788 (ref. 81). The combined grids of 270 m and about 8 km can be found at https://doi.org/10.6084/m9.figshare.24850734 (ref. 82). The Landsat NDVI (EVI), MODIS NDVI (EVI), DEM (including elevation, slope and aspect) and TerraClimate database (including precipitation and PDSI product) were calculated on GEE, which is available at https://code.earthengine.google.com/. The GIMMS NDVI data can be obtained from https://poles.tpdc.ac.cn/en/data/9775f2b4-7370-4e5e-a537-3482c9a83d88/. The land cover data were downloaded from http://maps.elie.ucl.ac.be/CCI/viewer/. The world continental boundaries were obtained from https://hub.arcgis.com/datasets/esri::world-continents/about. The sub-metre high-resolution satellite images were downloaded from Google Earth, which is available at https://earth.google.com/. The SPEI data are available from https://digital.csic.es/handle/10261/202305. The precipitation data can be retrieved from https://data.ceda.ac.uk/badc/cru/data/cru_ts. The available water-storage capacity, soil clay and soil sand data were downloaded from https://daac.ornl.gov/SOILS/guides/HWSD.html. The canopy height can be obtained from https://webmap.ornl.gov/ogc/dataset.jsp?dg_id=10023_1. The global maximum rooting depth was derived from https://wci.earth2observe.eu/thredds/catalog/usc/root-depth/catalog.html. The tree density was derived from https://elischolar.library.yale.edu/yale_fes_data/1/. The native plant species richness was downloaded from https://anthroecology.org/.

Code availability

Java, MATLAB, Python and R codes for the analysis of these data can be obtained from https://github.com/YCY-github-YCY/Tree.

References

1. IPCC. *Climate Change 2022: Impacts, Adaptation and Vulnerability* (eds Pörtner, H.-O. et al.) (Cambridge Univ, Press, 2022).
2. McDowell, N. G. et al. Pervasive shifts in forest dynamics in a changing world. *Science* **368**, z9463 (2020).
3. Allen, C. D. et al. A global overview of drought and heat-induced tree mortality reveals emerging climate change risks for forests. *For. Ecol. Manag.* **259**, 660–684 (2010).
4. Allen, C. D., Breshears, D. D. & McDowell, N. G. On underestimation of global vulnerability to tree mortality and forest die-off from hotter drought in the Anthropocene. *Ecosphere* **6**, 1–55 (2015).
5. Hartmann, H. et al. Research frontiers for improving our understanding of drought-induced tree and forest mortality. *N. Phytol.* **218**, 15–28 (2018).
6. Williams, A. P. et al. Temperature as a potent driver of regional forest drought stress and tree mortality. *Nat. Clim. Change* **3**, 292–297 (2013).
7. Hammond, W. M. et al. Global field observations of tree die-off reveal hotter-drought fingerprint for Earth's forests. *Nat. Commun.* **13**, 1761 (2022).
8. Anderegg, W. R. et al. Pervasive drought legacies in forest ecosystems and their implications for carbon cycle models. *Science* **349**, 528–532 (2015).
9. Doughty, C. E. et al. Drought impact on forest carbon dynamics and fluxes in Amazonia. *Nature* **519**, 78–82 (2015).
10. Gatti, L. V. et al. Drought sensitivity of Amazonian carbon balance revealed by atmospheric measurements. *Nature* **506**, 76–80 (2014).
11. Lewis, S. L. et al. The 2010 Amazon drought. *Science* **331**, 554 (2011).
12. Phillips, O. L. et al. Drought sensitivity of the Amazon rainforest. *Science* **323**, 1344–1347 (2009).
13. Peñuelas, J. et al. Shifting from a fertilization-dominated to a warming-dominated period. *Nat. Ecol. Evol.* **1**, 1438–1445 (2017).
14. Chen, C. et al. China and India lead in greening of the world through land-use management. *Nat. Sustain.* **2**, 122–129 (2019).
15. Myneni, R. B. et al. Increased plant growth in the northern high latitudes from 1981 to 1991. *Nature* **386**, 698–702 (1997).
16. Piao, S. et al. Characteristics, drivers and feedbacks of global greening. *Nat. Rev. Earth Environ.* **1**, 14–27 (2020).
17. Zhu, Z. et al. Greening of the Earth and its drivers. *Nat. Clim. Change* **6**, 791–795 (2016).

18. Friedlingstein, P. et al. Global carbon budget 2021. *Earth Syst. Sci. Data* **14**, 1917–2005 (2022).
19. Qiao, X. et al. Latitudinal patterns of forest ecosystem stability across spatial scales as affected by biodiversity and environmental heterogeneity. *Glob. Chang. Biol.* **29**, 2242–2255 (2023).
20. Qiao, X. et al. Spatial asynchrony matters more than alpha stability in stabilizing ecosystem productivity in a large temperate forest region. *Glob. Ecol. Biogeogr.* **31**, 1133–1146 (2022).
21. Peng, X. et al. Northern Hemisphere greening in association with warming permafrost. *J. Geophys. Res. Biogeosci.* **125**, e2019JG005086 (2020).
22. Piao, S. et al. Evidence for a weakening relationship between interannual temperature variability and northern vegetation activity. *Nat. Commun.* **5**, 5018 (2014).
23. Wu, X. et al. Higher temperature variability reduces temperature sensitivity of vegetation growth in Northern Hemisphere. *Geophys. Res. Lett.* **44**, 6173–6181 (2017).
24. Lundberg, S. M. & Lee, S.-I. A unified approach to interpreting model predictions. In *Proc. 31st International Conference on Neural Information Processing Systems* (eds von Luxburg, U. et al.) 4768–4777 (2017).
25. Lundberg, S. M. et al. From local explanations to global understanding with explainable AI for trees. *Nat. Mach. Intell.* **2**, 56–67 (2020).
26. Grossiord, C. Having the right neighbors: how tree species diversity modulates drought impacts on forests. *N. Phytol.* **228**, 42–49 (2020).
27. O'Brien, M. J., Reynolds, G., Ong, R. & Hector, A. Resistance of tropical seedlings to drought is mediated by neighbourhood diversity. *Nat. Ecol. Evol.* **1**, 1643–1648 (2017).
28. Giardina, F. et al. Tall Amazonian forests are less sensitive to precipitation variability. *Nat. Geosci.* **11**, 405–409 (2018).
29. Stephenson, N. L. & Das, A. J. Height-related changes in forest composition explain increasing tree mortality with height during an extreme drought. *Nat. Commun.* **11**, 3402 (2020).
30. Wu, H., Franklin, S. B., Liu, J. & Lu, Z. Relative importance of density dependence and topography on tree mortality in a subtropical mountain forest. *For. Ecol. Manag.* **384**, 169–179 (2017).
31. Adams, H. R., Barnard, H. R. & Loomis, A. K. Topography alters tree growth–climate relationships in a semi-arid forested catchment. *Ecosphere* **5**, 1–16 (2014).
32. Ashcroft, M. B., Chisholm, L. A. & French, K. O. Climate change at the landscape scale: predicting fine-grained spatial heterogeneity in warming and potential refugia for vegetation. *Glob. Chang. Biol.* **15**, 656–667 (2009).
33. Keppel, G. et al. Refugia: identifying and understanding safe havens for biodiversity under climate change. *Glob. Ecol. Biogeogr.* **21**, 393–404 (2012).
34. McDowell, N. G. et al. Mechanisms of a coniferous woodland persistence under drought and heat. *Environ. Res. Lett.* **14**, 45014 (2019).
35. Serra-Diaz, J. M., Scheller, R. M., Syphard, A. D. & Franklin, J. Disturbance and climate microrefugia mediate tree range shifts during climate change. *Landsc. Ecol.* **30**, 1039–1053 (2015).
36. Ashcroft, M. B., Gollan, J. R., Warton, D. I. & Ramp, D. A novel approach to quantify and locate potential microrefugia using topoclimate, climate stability, and isolation from the matrix. *Glob. Chang. Biol.* **18**, 1866–1879 (2012).
37. Dobrowski, S. Z. A climatic basis for microrefugia: the influence of terrain on climate. *Glob. Chang. Biol.* **17**, 1022–1035 (2011).
38. Keppel, G. et al. The capacity of refugia for conservation planning under climate change. *Front. Ecol. Environ.* **13**, 106–112 (2015).
39. Schwendenmann, L. et al. Tree water uptake in a tropical plantation varying in tree diversity: interspecific differences, seasonal shifts and complementarity. *Ecohydrology* **8**, 1–12 (2015).
40. West, A. G. et al. Diverse functional responses to drought in a Mediterranean-type shrubland in South Africa. *N. Phytol.* **195**, 396–407 (2012).
41. Lebourgeois, F., Gomez, N., Pinto, P. & Mérian, P. Mixed stands reduce Abies alba tree-ring sensitivity to summer drought in the Vosges mountains, western Europe. *For. Ecol. Manag.* **303**, 61–71 (2013).
42. Oliveira, B. F. & Scheffers, B. R. Vertical stratification influences global patterns of biodiversity. *Ecography* **42**, 249 (2019).
43. Morin, X. et al. Temporal stability in forest productivity increases with tree diversity due to asynchrony in species dynamics. *Ecol. Lett.* **17**, 1526–1535 (2014).
44. Ouyang, S. et al. Stability in subtropical forests: the role of tree species diversity, stand structure, environmental and socio-economic conditions. *Glob. Ecol. Biogeogr.* **30**, 500–513 (2021).
45. Schnabel, F. et al. Species richness stabilizes productivity via asynchrony and drought-tolerance diversity in a large-scale tree biodiversity experiment. *Sci. Adv.* **7**, k1643 (2021).
46. Kemppinen, J. et al. Consistent trait–environment relationships within and across tundra plant communities. *Nat. Ecol. Evol.* **5**, 458–467 (2021).
47. Sitch, S. et al. Evaluation of the terrestrial carbon cycle, future plant geography and climate-carbon cycle feedbacks using five dynamic global vegetation models (DGVMs). *Glob. Chang. Biol.* **14**, 2015–2039 (2008).
48. Khoury, S. & Coomes, D. A. Resilience of Spanish forests to recent droughts and climate change. *Glob. Chang. Biol.* **26**, 7079–7098 (2020).
49. Forzieri, G. et al. Emerging signals of declining forest resilience under climate change. *Nature* **608**, 534–539 (2022).
50. Rogers, B. M. et al. Detecting early warning signals of tree mortality in boreal North America using multiscale satellite data. *Glob. Chang. Biol.* **24**, 2284–2304 (2018).
51. Pinzon, J. E. & Tucker, C. J. A non-stationary 1981–2012 AVHRR NDVI3g time series. *Remote Sens.* **6**, 6929–6960 (2014).
52. Holben, B. N. Characteristics of maximum-value composite images from temporal AVHRR data. *Int. J. Remote Sens.* **7**, 1417–1434 (1986).
53. Masek, J. G. et al. A Landsat surface reflectance dataset for North America, 1990-2000. *IEEE Geosci. Remote S.* **3**, 68–72 (2006).
54. Vermote, E & Saleous, N. *LEDAPS Surface Reflectance Product Description* (University of Maryland, 2007).
55. Vermote, E., Justice, C., Claverie, M. & Franch, B. Preliminary analysis of the performance of the Landsat 8/OLI land surface reflectance product. *Remote Sens. Environ.* **185**, 46–56 (2016).
56. Foga, S. et al. Cloud detection algorithm comparison and validation for operational Landsat data products. *Remote Sens. Environ.* **194**, 379–390 (2017).
57. Roy, D. P. et al. Characterization of Landsat-7 to Landsat-8 reflective wavelength and normalized difference vegetation index continuity. *Remote Sens. Environ.* **185**, 57–70 (2016).
58. Amani, M. et al. Google Earth Engine cloud computing platform for remote sensing big data applications: a comprehensive review. *IEEE J. Sel. Top. Appl. Earth Obs. Remote Sens.* **13**, 5326–5350 (2020).
59. Gorelick, N. et al. Google Earth Engine: planetary-scale geospatial analysis for everyone. *Remote Sens. Environ.* **202**, 18–27 (2017).
60. Tamiminia, H. et al. Google Earth Engine for geo-big data applications: a meta-analysis and systematic review. *ISPRS J. Photogramm.* **164**, 152–170 (2020).

61. Abatzoglou, J. T., Dobrowski, S. Z., Parks, S. A. & Hegewisch, K. C. TerraClimate, a high-resolution global dataset of monthly climate and climatic water balance from 1958–2015. *Sci. Data* **5**, 1–12 (2018).
62. Vicente-Serrano, S. M. et al. A global 0.5 gridded dataset (1901–2006) of a multi-scalar drought index considering the joint effects of precipitation and temperature. *J. Hydrometeorol.* **11**, 1033–1043 (2010).
63. Tong, X. et al. Increased vegetation growth and carbon stock in China karst via ecological engineering. *Nat. Sustain.* **1**, 44–50 (2018).
64. Harris, I., Jones, P. D., Osborn, T. J. & Lister, D. H. Updated high-resolution grids of monthly climatic observations-the CRU TS3. 10 Dataset. *Int. J. Climatol.* **34**, 623–642 (2014).
65. Wieder, W. R., Boehnert, J., Bonan, G. B. & Langseth, M. Regridded Harmonized World Soil Database v1.2 https://doi.org/10.3334/ORNLDAAC/1247 (Oak Ridge National Laboratory Distributed Active Archive Center, 2014).
66. Simard, M., Pinto, N., Fisher, J. B. & Baccini, A. Mapping forest canopy height globally with spaceborne lidar. *J. Geophys. Res. Biogeosci.* **116**, 4021 (2011).
67. Crowther, T. W. et al. Mapping tree density at a global scale. *Nature* **525**, 201–205 (2015).
68. Ellis, E. C., Antill, E. C. & Kreft, H. All is not loss: plant biodiversity in the Anthropocene. *PLoS One* **7**, e30535 (2012).
69. Anderegg, W. R. et al. Hydraulic diversity of forests regulates ecosystem resilience during drought. *Nature* **561**, 538–541 (2018).
70. Hamed, K. H. & Rao, A. R. A modified Mann–Kendall trend test for autocorrelated data. *J. Hydrol.* **204**, 182–196 (1998).
71. Yang, H. et al. The detection and attribution of extreme reductions in vegetation growth across the global land surface. *Glob. Chang. Biol.* **29**, 2351–2362 (2023).
72. Batunacun, W. R., Lakes, T. & Nendel, C. Using Shapley additive explanations to interpret extreme gradient boosting predictions of grassland degradation in Xilingol, China. *Geosci. Model Dev.* **14**, 1493–1510 (2021).
73. Odebiri, O., Mutanga, O., Odindi, J. & Naicker, R. Modelling soil organic carbon stock distribution across different land-uses in South Africa: a remote sensing and deep learning approach. *ISPRS J. Photogramm.* **188**, 351–362 (2022).
74. Silva, S. J., Keller, C. A. & Hardin, J. Using an explainable machine learning approach to characterize Earth System Model errors: application of SHAP analysis to modeling lightning flash occurrence. *J. Adv. Model. Earth Syst.* **14**, e2021MS002881 (2022).
75. Wang, H. et al. Exploring complex water stress–gross primary production relationships: impact of climatic drivers, main effects, and interactive effects. *Glob. Chang. Biol.* **28**, 4110–4123 (2022).
76. Zhu, P., Abramoff, R., Makowski, D. & Ciais, P. Uncovering the past and future climate drivers of wheat yield shocks in Europe with machine learning. *Earths Future* **9**, e2020EF001815 (2021).
77. Chen, T. & Guestrin, C. XGBoost: a scalable tree boosting system. In *Proc. 22nd ACM SIGKDD International Conference on Knowledge Discovery and Data Mining* (eds Krishnapuram, B. et al.) 785–794 (2016).
78. Zuur, A. F., Ieno, E. N. & Elphick, C. S. A protocol for data exploration to avoid common statistical problems. *Methods Ecol. Evol.* **1**, 3–14 (2010).
79. Yan, Y. et al. Tree-mortality sites for 'Climate-induced tree mortality pulses are obscured by broad-scale and long-term greening'. Figshare https://doi.org/10.6084/m9.figshare.24847698 (2023).
80. Yan, Y. et al. Google Earth sub-metre high-resolution satellite images for 'Climate-induced tree mortality pulses are obscured by broad-scale and long-term greening'. Figshare https://doi.org/10.6084/m9.figshare.23243915 (2023).
81. Yan, Y. et al. Climate, vegetation and soil data for 'Climate-induced tree mortality pulses are obscured by broad-scale and long-term greening'. Figshare https://doi.org/10.6084/m9.figshare.24847788 (2023).
82. Yan, Y. et al. Combined grids of 270 m and about 8 km for 'Climate-induced tree mortality pulses are obscured by broad-scale and long-term greening'. Figshare https://doi.org/10.6084/m9.figshare.24850734 (2023).

Acknowledgements

This study was supported by the National Natural Science Foundation of China (grant no. 41988101 to S.P.). A.C. was supported by a US Department of Energy grant (grant no. DE-SC0022074). We thank D. Zhu, W. Lang, Y. Yan and Y. Deng for their useful suggestions for this paper, and H. Zhuang and M. Li for their help with the experiments. Any use of trade, product or firm names in this paper is for descriptive purposes only and does not imply endorsement by the US government.

Author contributions

S.P. designed the research. Y.Y. performed analysis and drafted the figures. Y.Y., S.P., S.H. and A.C. wrote the first draft of the manuscript. W.M.H. collected the tree-mortality sites. C.D.A., W.M.H., S.M.M., R.B.M. and H.X. revised the manuscript. All authors contributed to the interpretation of the results and to the text.

Competing interests

The authors declare no competing interests.

Additional information

Supplementary information The online version contains supplementary material available at https://doi.org/10.1038/s41559-024-02372-1.

Correspondence and requests for materials should be addressed to Shilong Piao or Anping Chen.

Peer review information *Nature Ecology & Evolution* thanks the anonymous reviewers for their contribution to the peer review of this work.

nature portfolio

Corresponding author(s): Shilong Piao

Last updated by author(s): Dec 21, 2023

Reporting Summary

Nature Portfolio wishes to improve the reproducibility of the work that we publish. This form provides structure for consistency and transparency in reporting. For further information on Nature Portfolio policies, see our Editorial Policies and the Editorial Policy Checklist.

Statistics

For all statistical analyses, confirm that the following items are present in the figure legend, table legend, main text, or Methods section.

n/a	Confirmed
☐	☒ The exact sample size (*n*) for each experimental group/condition, given as a discrete number and unit of measurement
☐	☒ A statement on whether measurements were taken from distinct samples or whether the same sample was measured repeatedly
☐	☒ The statistical test(s) used AND whether they are one- or two-sided *Only common tests should be described solely by name; describe more complex techniques in the Methods section.*
☐	☒ A description of all covariates tested
☐	☒ A description of any assumptions or corrections, such as tests of normality and adjustment for multiple comparisons
☐	☒ A full description of the statistical parameters including central tendency (e.g. means) or other basic estimates (e.g. regression coefficient) AND variation (e.g. standard deviation) or associated estimates of uncertainty (e.g. confidence intervals)
☐	☒ For null hypothesis testing, the test statistic (e.g. *F*, *t*, *r*) with confidence intervals, effect sizes, degrees of freedom and *P* value noted *Give P values as exact values whenever suitable.*
☒	☐ For Bayesian analysis, information on the choice of priors and Markov chain Monte Carlo settings
☐	☒ For hierarchical and complex designs, identification of the appropriate level for tests and full reporting of outcomes
☒	☐ Estimates of effect sizes (e.g. Cohen's *d*, Pearson's *r*), indicating how they were calculated

Our web collection on statistics for biologists contains articles on many of the points above.

Software and code

Policy information about availability of computer code

Data collection	No software was used to collect data.
Data analysis	The analyses and mapping were both performed using Google earth engine (JavaScript), ArcGIS 10.7, MATLAB (R2020b), Pycharm 2017.2.7, and Rstudio (R version 4.0.3). Codes for processing and analyzing these data can be found in Github (https://github.com/YCY-github-YCY/Tree).C Function of Mask (CFMASK) algorithm is a cloud masking algorithm available in Google Earth Engine.

For manuscripts utilizing custom algorithms or software that are central to the research but not yet described in published literature, software must be made available to editors and reviewers. We strongly encourage code deposition in a community repository (e.g. GitHub). See the Nature Portfolio guidelines for submitting code & software for further information.

Data

Policy information about availability of data

All manuscripts must include a data availability statement. This statement should provide the following information, where applicable:

- Accession codes, unique identifiers, or web links for publicly available datasets
- A description of any restrictions on data availability
- For clinical datasets or third party data, please ensure that the statement adheres to our policy

The web links for publicly available datasets are present in the data availability statement of the paper. The codes for processing these data is available on GitHub at the following repository: https://github.com/YCY-github-YCY/Tree.

Research involving human participants, their data, or biological material

Policy information about studies with human participants or human data. See also policy information about sex, gender (identity/presentation), and sexual orientation and race, ethnicity and racism.

Reporting on sex and gender	N/A
Reporting on race, ethnicity, or other socially relevant groupings	N/A
Population characteristics	N/A
Recruitment	N/A
Ethics oversight	N/A

Note that full information on the approval of the study protocol must also be provided in the manuscript.

Field-specific reporting

Please select the one below that is the best fit for your research. If you are not sure, read the appropriate sections before making your selection.

☐ Life sciences ☐ Behavioural & social sciences ☒ Ecological, evolutionary & environmental sciences

For a reference copy of the document with all sections, see nature.com/documents/nr-reporting-summary-flat.pdf

Ecological, evolutionary & environmental sciences study design

All studies must disclose on these points even when the disclosure is negative.

Study description	Through analyzing 114,786 Landsat surface reflectance images and three satellite-based, Normalized Difference Vegetation Index (NDVI) datasets with spatial resolutions that range from 30 m to 8 km for 1,303 field-documented sites of severe tree mortality events across the globe, we demonstrate (1) consistent greening trends in growing-season NDVI (NDVIGS) across all spatial resolutions over long time-scales (a decade or longer); (2) topographical and forest diversity mitigate the impact of severe tree mortality.
Research sample	The global dataset of tree mortality sites used in this study was obtained from a meta-analysis of previously reported tree mortality events. This dataset records the geo-referenced locations of 1,303 vegetation sites that document the timing of tree mortality events resulting from extreme drought and heat stress from 1970-2018, which were collected from 154 peer-reviewed studies.
Sampling strategy	N/A
Data collection	The Landsat NDVI (EVI), MODIS NDVI (EVI), DEM (elevation, slope, and aspect), and TerraClimate database (including precipitation and PDSI product) are calculated on Google earth engine, which is available at https://code.earthengine.google.com/. Other data sets were download from the URLs in the data availability statement in the main text.
Timing and spatial scale	We used 1,303 sites that document the timing of tree mortality events resulting from extreme drought and heat stress from 1970-2018. These sites encompass a wide range of forest types and climate zones across all the continents except Antarctica. For each of the 1,303 georeferenced sites, we calculated its corresponding mean value of Normalized Difference Vegetation Index of the growing season (NDVIGS) of each year from three commonly used satellite sensors that constitute a fine-to-coarse sequence in spatial resolution, including Landsat (30 m, 1984-2020), Moderate Resolution Imaging Spectroradiometer (MODIS, 250 m, 2000-2020), and Advanced Very High Resolution Radiometer (AVHRR, 8 km, 1984-2015).
Data exclusions	N/A
Reproducibility	Our analyses were based on publicly available satellite data, 1,303 geo-referenced tree mortality sites, and well-defined methods, and the results could be reliably reproduced.
Randomization	N/A
Blinding	N/A

Did the study involve field work? ☐ Yes ☒ No

Reporting for specific materials, systems and methods

We require information from authors about some types of materials, experimental systems and methods used in many studies. Here, indicate whether each material, system or method listed is relevant to your study. If you are not sure if a list item applies to your research, read the appropriate section before selecting a response.

Materials & experimental systems

n/a	Involved in the study
☒	☐ Antibodies
☒	☐ Eukaryotic cell lines
☒	☐ Palaeontology and archaeology
☒	☐ Animals and other organisms
☒	☐ Clinical data
☒	☐ Dual use research of concern
☒	☐ Plants

Methods

n/a	Involved in the study
☒	☐ ChIP-seq
☒	☐ Flow cytometry
☒	☐ MRI-based neuroimaging

Plants

Seed stocks	N/A
Novel plant genotypes	N/A
Authentication	N/A